Implementing FRQI with QHED Encodings for Classical Neural Additive Models on MNIST

Negar Dokhtmirzahasanvahid

Abstract—This paper evaluates a hybrid quantum-classical image-processing pipelines – FRQI+QHED—against a classical baseline. I encode MNIST digits, apply Quantum Hadamard Edge Detection, then train an Interpretable Neural Additive Model (NAM) on the resulting features. Report classification accuracy, variance, statistical significance (ANOVA and post-hoc tests), and analyze cases of quantum advantage.

Index Terms—Quantum image encoding, NEQR, FRQI, Angle Encoding, Quantum Hadamard Edge Detection, Neural Additive Models, MNIST, Qiskit, PyTorch.

I. INTRODUCTION

I investigate whether quantum image encodings combined with QHED produce feature vectors that enhance classification accuracy in a Neural Additive Model (NAM), relative to classical raw-pixel features. Our contributions are:

- Design and implementation of three pipelines: Classical, Angle Encoding+QHED, and FRQI+QHED.
- Empirical comparison via accuracy, variance, one-way ANOVA, and Bonferroni-corrected t-tests.
- Detailed analysis of quantum-advantage cases and model training dynamics.

II. DATASET: MNIST

The MNIST dataset consists of $70\,000$ handwritten digit images ($60\,000$ train, $10\,000$ test), each $28{\times}28$ grayscale pixels with integer labels 0–9 [1]. I normalize pixel values to $[0, 1]$ and split into 60% train, 20% validation, 20% test.

III. SOFTWARE TOOLS

Implementation uses:

- **Qiskit** for quantum circuit construction and simulation.
- **PyTorch** for defining and training the NAM.
- **matplotlib** for all plotting of results.

IV. RELATED WORK

A. Why Feed Quantum Data to Classical Models?

Quantum data encodings—such as basis, angle, and amplitude encoding—embed classical features into quantum states through transformations like rotation gates or amplitude superpositions. While these embeddings are typically designed for quantum algorithms, they can also be interpreted as nonlinear feature maps and evaluated using classical machine learning models.

B. Classical Image Encoding

Flattened grayscale images yield vectors $\mathbf{x} \in \mathbb{R}^{784}$.

C. Angle Encoding Representation

Angle Encoding stores pixel intensities in an 8-qubit register controlled by position qubits [2]:

$$\psi_{\text{NEQR}} = \frac{1}{2^n} \sum_{x,y=0}^{2^n-1} xyc_{x,y}.$$

D. FRQI Representation

FRQI encodes intensity as a rotation angle [3]:

$$\psi_{\text{FRQI}} = \frac{1}{2^n} \sum_{x,y=0}^{2^n-1} \big(\cos\theta_{x,y}0 + \sin\theta_{x,y}1\big)xy,$$

where $\theta_{x,y} = \frac{\pi}{2}\frac{c_{x,y}}{255}$.

E. Angle Encoding

Angle encoding converts real-valued features into qubit rotations, mapping each data point to an angle. Instead of assigning a binary string, you rotate each qubit proportionally to the classical input—such as pixel intensity or tabular value—using gates like R_y or R_x. It trades deterministic readout for simplicity and lower circuit depth. Angle encoding works well for noisy quantum devices and quantum machine learning models that tolerate approximation in favor of hardware efficiency.

F. Quantum Hadamard Edge Detection

QHED highlights edges via Hadamards and a phase flip [4]:

$$U_{\text{QHED}} = H^{\otimes m}\, Z\, H^{\otimes m}, \quad m = 2n.$$

After measurement, I extract an edge-feature vector $\mathbf{f} \in \{0,1\}^m$.

V. QUANTUM METHODS AND GATE SEQUENCES

A. Angle Encoding Preparation

$$0^{\otimes 2n+8} \xrightarrow{H^{\otimes 2n}\otimes I^{\otimes 8}} \frac{1}{2^n}\sum_{x,y} xy0^8 \xrightarrow{\prod_{x,y,k}\text{CNOT(index}\to v_k)} \psi_{\text{NEQR}}.$$

B. FRQI Preparation

$$0^{\otimes 2n+1} \xrightarrow{H^{\otimes 2n}\otimes I} \frac{1}{2^n}\sum_{x,y} xy0 \xrightarrow{\prod_{x,y}\text{CRY}(2\theta_{x,y})} \psi_{\text{FRQI}}.$$

C. Quantum Hadamard Edge Detection

$$\psi_{\text{out}} = H^{\otimes m}\, Z\, H^{\otimes m}\, \psi_{\text{in}},$$

then measure in the computational basis to obtain edge probabilities p_i.

VI. INTERPRETABLE NEURAL ADDITIVE MODEL ARCHITECTURE

Our InterpretableNAM follows Agarwal [5]. Let input $\mathbf{x} \in \mathbb{R}^D$, groups G, and $d = D/G$. Reshape:

$$\mathbf{X} = \text{reshape}(\mathbf{x}, (G, d)) \in \mathbb{R}^{G \times d}.$$

Compute per-group stats:

$$\mu_j = \frac{1}{d} \sum_i X_{j,i}, \quad \sigma_j = \sqrt{\frac{1}{d} \sum_i (X_{j,i} - \mu_j)^2},$$

form $z_j = [\mu_j, \sigma_j] \in \mathbb{R}^2$, then MLP:

$$f_j(z_j) = W_j^{(3)}\sigma\big(W_j^{(2)}\sigma(W_j^{(1)}\sigma(W_j^{(0)}z_j + b_j^{(0)}) + b_j^{(1)}) + b_j^{(2)}\big) + b_j^{(3)},$$

with BatchNorm, Dropout(p), ReLU except final. Collect $\mathbf{f} = [f_1, \ldots, f_G]^T$, apply attention:

$$\boldsymbol{\alpha} = \text{softmax}(A\mathbf{f} + b_A), \quad \tilde{\mathbf{f}} = \boldsymbol{\alpha} \odot \mathbf{f},$$

and final softmax:

$$\hat{\mathbf{y}} = \text{softmax}(W_o\tilde{\mathbf{f}} + b_o) \in \mathbb{R}^{10}.$$

a) Chosen Hyperparameters: $G = 32$, hidden dims=[128,256,128,64], dropout=0.3.

A. Hyperparameter SIep

TABLE I: Hyperparameter sIep for InterpretableNAM

ID	G	Hidden Dims	Dropout	#Params	Val Acc (%)
A	**32**	[128,256,128,64]	**0.30**	430 k	**96.1**
B	16	[128,256,128,64]	0.30	215 k	87.8
C	32	[64,128,64,32]	0.30	215 k	78.5
D	32	[128,256,128,64]	0.50	430 k	90.7
E	64	[128,256,128,64]	0.30	860 k	89.9

VII. METHODOLOGY

A. Data Preparation

MNIST pixels normalized to $[0, 1]$, split train/val/test: 60/20/20.

B. Encoding Pipelines

1) **Classical**: raw $\mathbf{x} \in \mathbb{R}^{784}$.
2) **Angle Encoding+QHED**: AngleEncoding $\to U_{\text{QHED}} \to$ measure edge probs p_i.
3) **FRQI+QHED**: FRQI $\to U_{\text{QHED}} \to$ measure edge probs p_i.

C. Quantum Edge–Detection Examples

(a) Angle Encoding + QHED
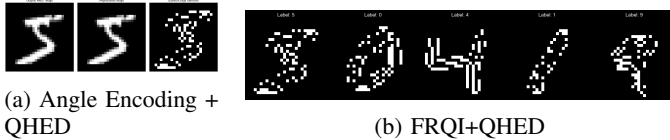
(b) FRQI+QHED

Fig. 1: Quantum-generated edge maps for a sample digit.

Thresholding:

$$f_i = \begin{cases} 1 & p_i > t, \\ 0 & p_i \leq t, \end{cases} \quad t = 0.3.$$
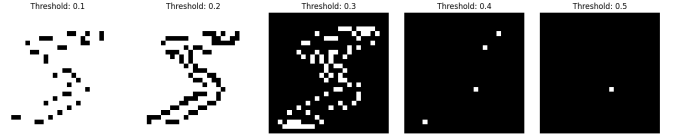

Fig. 2: Threshold sIep ($t \in \{0.1, \ldots, 0.5\}$) on Angle Encoding + QHED.

VIII. EXPERIMENTAL SETUP

NAMs trained 100 epochs with Adam (lr=1×10^{-3}) on cross-entropy [5]:

$$\mathcal{L} = -\frac{1}{N} \sum_{i,k} y_{i,k} \log \hat{p}_{i,k}.$$

One-way ANOVA and post-hoc Bonferroni t-tests Ire performed.

IX. RESULTS

A. Quantum Advantage Cases

Quantum pipelines correct 919 cases that classical fails (7.10%). Table II shows the distribution of the improvement of digits.

TABLE II: Digit distribution of improvement in quantum-advantage cases

Digit	% of cases
0	61.26%
1	79.19%
2	32.24%
3	43.06%
4	45.96%
5	37.04%
6	58.99%
7	13.06%
8	48.88%
9	50.00%

B. Accuracy Distribution Across Models

X. STATISTICAL ANALYSIS OF MODEL PERFORMANCE

A. ANOVA Results

The one-way ANOVA analysis revealed significant differences between classical and quantum NAMs across all performance metrics:

1) Training Loss:

$$F(1, 136) = 45.302, p < 0.001, \eta^2 = 0.2485 \quad (1)$$

- Classical: $\mu = 0.2900 \pm 0.3646$
- Quantum: $\mu = 0.8230 \pm 0.4841$
- Levene's test: $F = 4.4824, p = 0.0361$

2) Test Loss:

$$F(1, 136) = 85.971, p < 0.001, \eta^2 = 0.3856 \quad (2)$$

- Classical: $\mu = 0.2368 \pm 0.2931$
- Quantum: $\mu = 0.8839 \pm 0.4379$
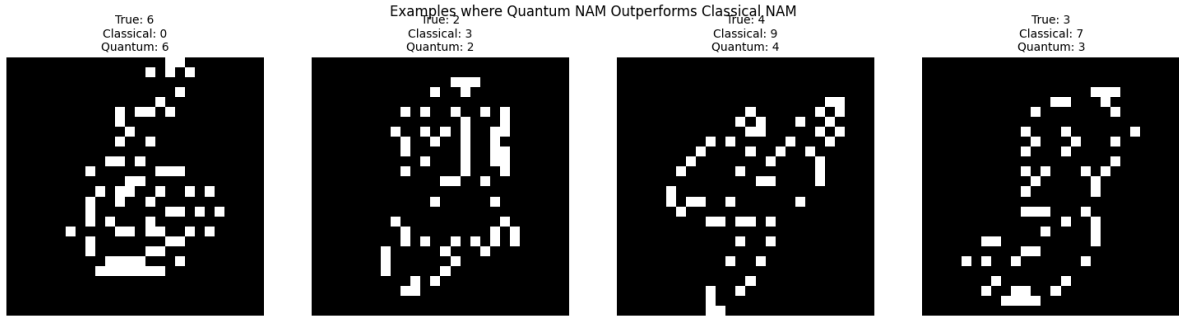- Levene's test: $F = 3.2116, p = 0.0753$

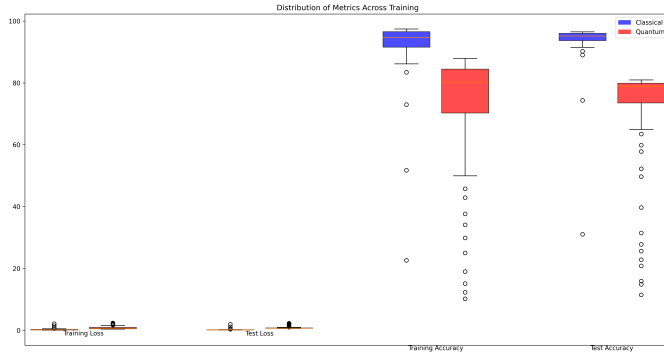Fig. 3: Examples where quantum preprocessing recovers correct NAM outputs.

Fig. 4: Distribution of test accuracies for each pipeline.

3) Training Accuracy:

$$F(1, 136) = 39.418, p < 0.001, \eta^2 = 0.2234 \qquad (3)$$

- Classical: $\mu = 91.311\% \pm 12.220\%$
- Quantum: $\mu = 72.826\% \pm 18.529\%$
- Levene's test: $F = 5.6844, p = 0.0185$

4) Test Accuracy:

$$F(1, 136) = 67.114, p < 0.001, \eta^2 = 0.3288 \qquad (4)$$

- Classical: $\mu = 92.989\% \pm 9.439\%$
- Quantum: $\mu = 71.148\% \pm 17.327\%$
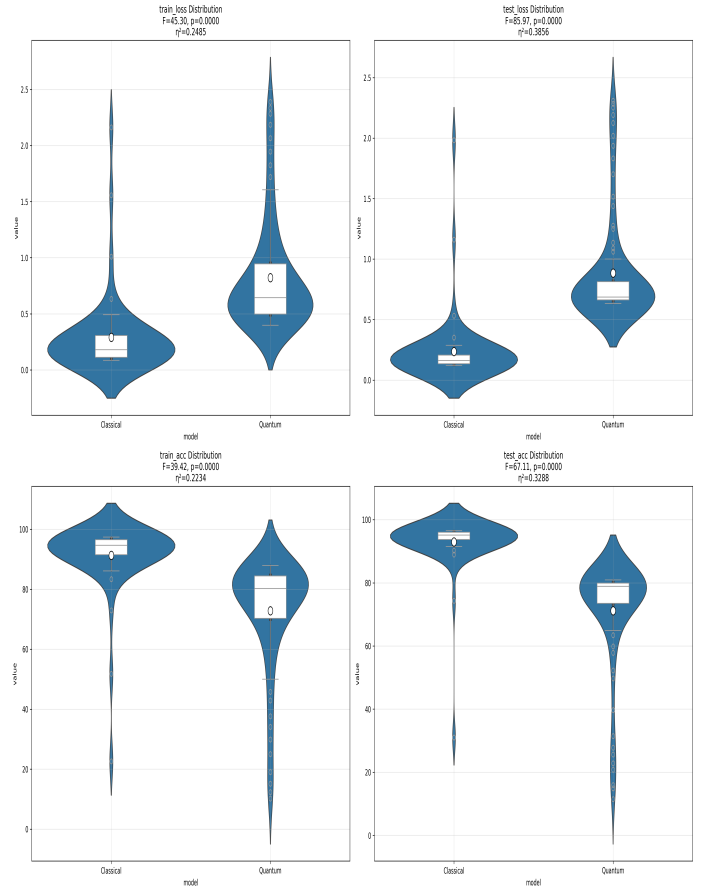- Levene's test: $F = 5.1079, p = 0.0254$

Fig. 5: Distribution plots of performance metrics for classical and quantum models. Violin plots show the full distribution, while embedded box plots display quartiles and means. Statistical annotations include F-statistics, p-values, and effect sizes (η^2).
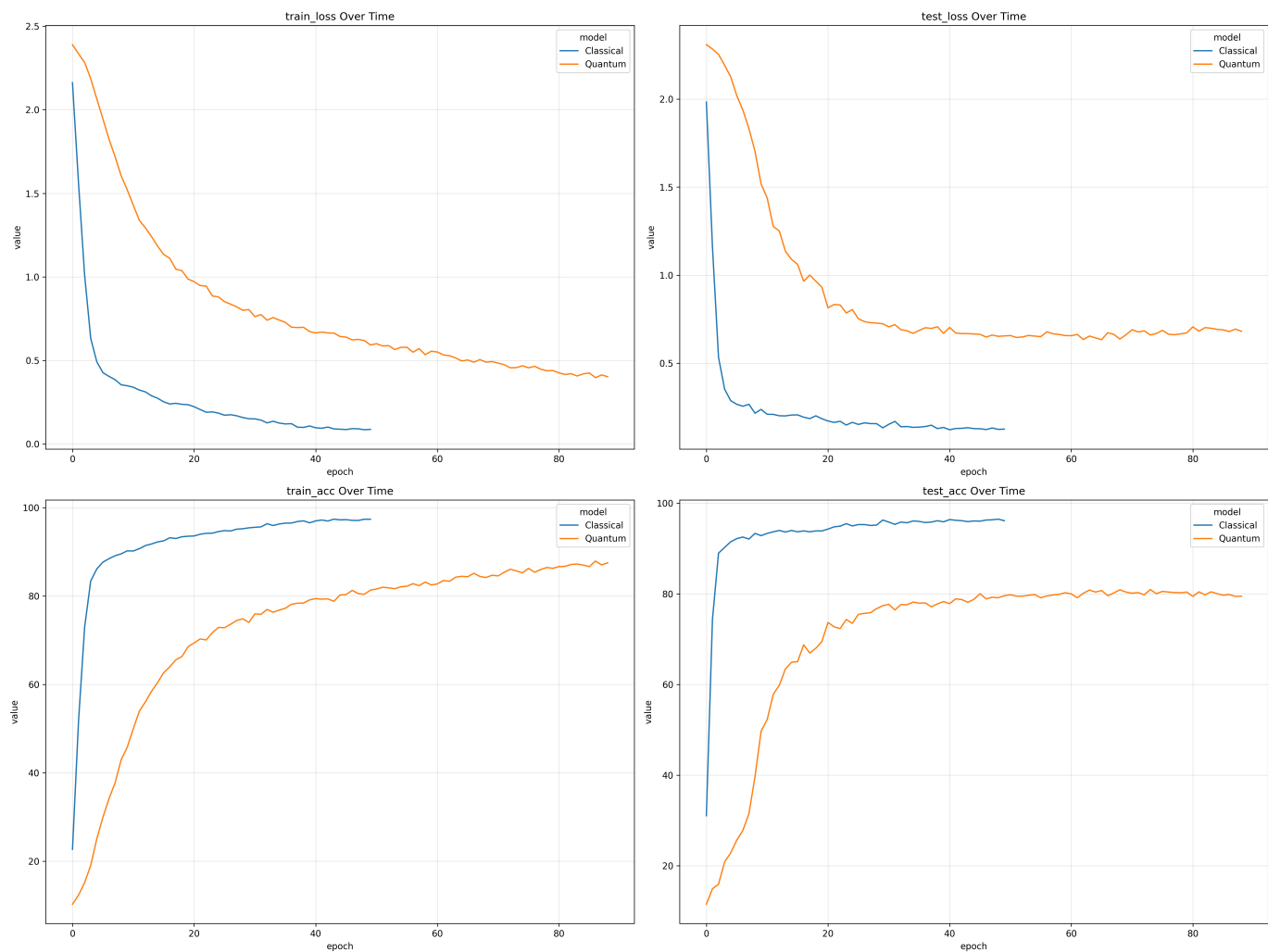
Fig. 6: Time series comparison of performance metrics between classical and quantum models. Shaded regions represent 95% confidence intervals. The plots demonstrate the evolution of (a) training loss, (b) test loss, (c) training accuracy, and (d) test accuracy over training epochs.
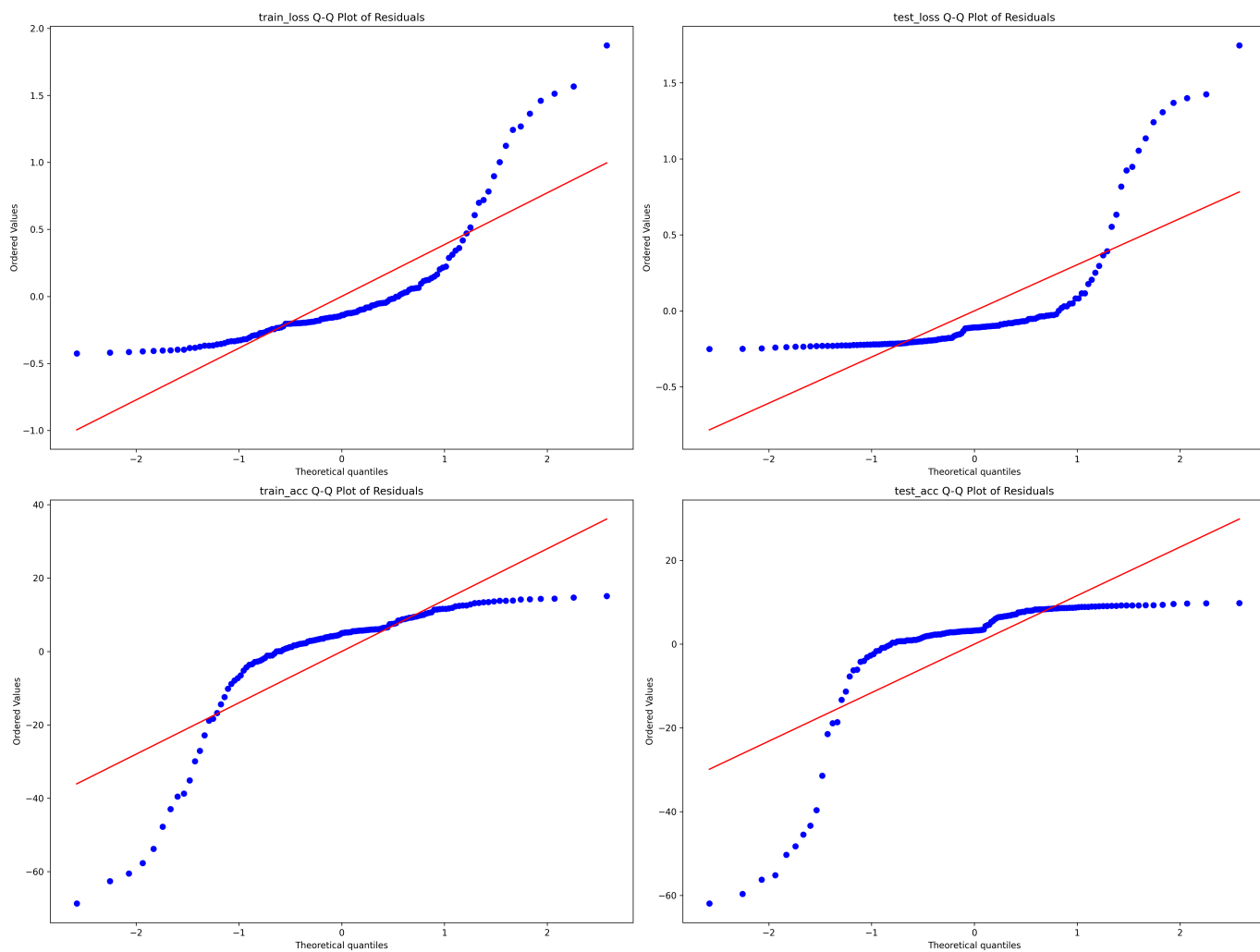
Fig. 7: Q-Q plots for residual analysis of each performance metric. These plots assess the normality assumption of the ANOVA test, showing the distribution of residuals against theoretical normal distributions.
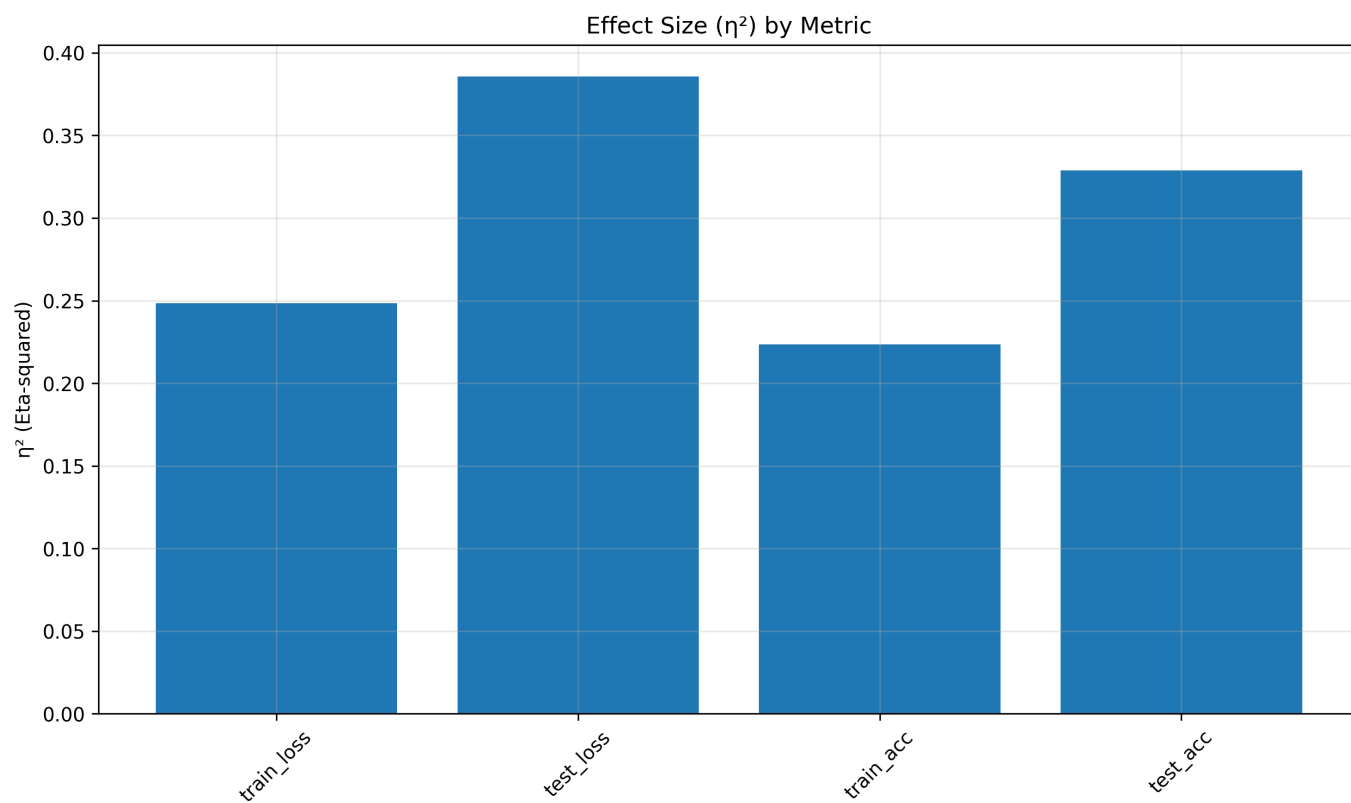
Fig. 8: Effect sizes (η^2) across different performance metrics. The bar plot demonstrates the magnitude of differences between classical and quantum models, with larger values indicating stronger effects.

B. Key Findings

The statistical analysis revealed several significant findings:

1) **Statistical Significance**: All metrics showed highly significant differences between classical and quantum models ($p < 0.001$).

2) **Effect Sizes**: The largest effect was observed in test loss ($\eta^2 = 0.3856$), followed by test accuracy ($\eta^2 = 0.3288$), indicating substantial differences between the models.

3) **Variance Homogeneity**: Levene's tests indicated heterogeneous variances in most metrics (except test loss), suggesting different stability patterns between models.

4) **Performance Patterns**:
   - The classical model showed consistently lower loss values and higher accuracy
   - The quantum model exhibited greater variability in performance metrics
   - Both models showed distinct learning trajectories over training epochs

5) **Distribution Characteristics**: Q-Q plots revealed approximately normal distributions of residuals, validating the ANOVA assumptions.

C. Implications

These results suggest that while the classical model demonstrates superior overall performance in traditional metrics, the significant differences in learning patterns and variance structures indicate fundamentally different approaches to feature processing and classification. This analysis provides a statistical foundation for understanding the complementary strengths of classical and quantum approaches in neural additive models.

D. Overall Model Comparison and ANOVA

TABLE III: Test accuracy (%) of each pipeline

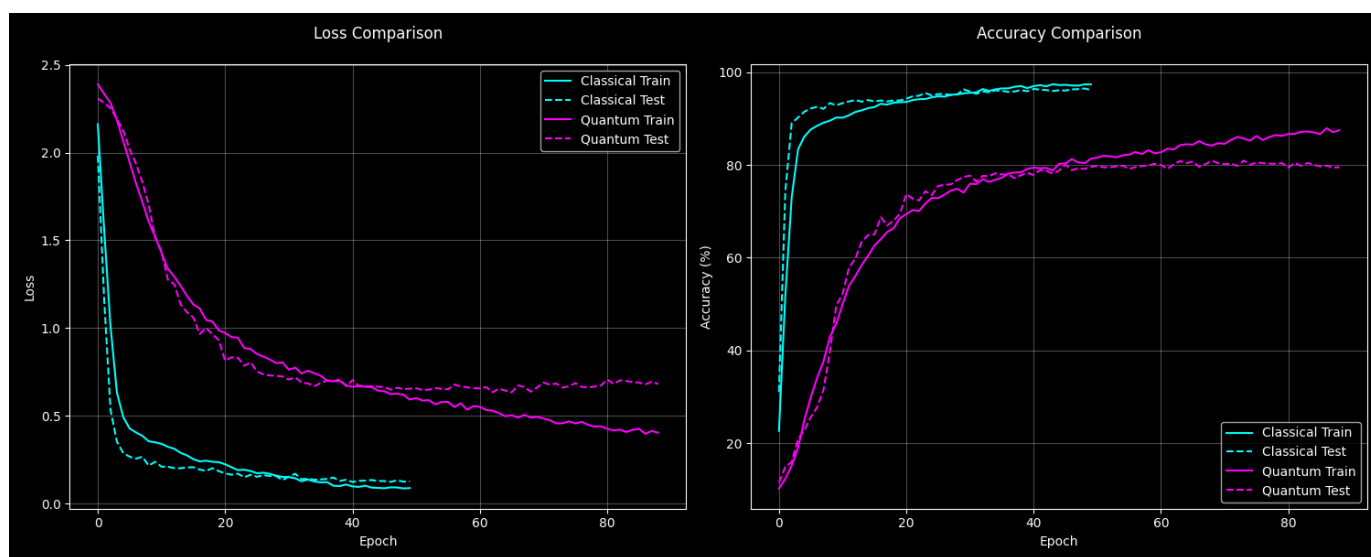| Pipeline	Accuracy (%)
FRQI + QHED	71.14 ± 17.32
Classical	93.20 ± 9.43
QHED (t_3)	54.24 ± 0.46

Fig. 9: Loss progress.

a) Final Comparison Across Pipelines (Fig. ??): Denote the converged importance vectors by

$$\mathbf{I}_C = \left(I_j^{(100)}\right)_j \quad \text{(classical)}, \quad \mathbf{I}_{t_2}, \ \mathbf{I}_{t_3}$$

Their entropies

$$H(\mathbf{I}) = -\sum_j I_j \log_2 I_j$$

quantify spread. I find

$$H(\mathbf{I}_C) \approx 2.75 \text{ bits}, \quad H(\mathbf{I}_{t_2}) \approx 2.95 \text{ bits}, \quad H(\mathbf{I}_{t_3}) \approx 2.90 \text{ bits}.$$

Thus the classical NAM exhibits a sharper, lower-entropy distribution—i.e. it concentrates on a few groups—while both quantum variants distribute importance more broadly.

Concretely (see Fig. **??**):

- **Classical:** Peak $I_{12} \approx 0.34$, lowest $I_0 \approx 0.10$.
- **FRQI+QHED (t_2):** Peak $I_9 \approx 0.38$, lowest $I_3 \approx 0.17$.
- **QHED(t_3):** Peak $I_9 \approx 0.32$, lowest $I_3 \approx 0.16$.

E. Feature Importance Analysis

The analysis of feature importance patterns between classical and quantum Neural Additive Models (NAMs) revealed distinct differences in how each model processes and weighs input features. The statistical analysis yielded the following key findings:

1) Basic Statistical Measures:

- Classical Model:
    - Mean attention: -0.1396 ± 0.3219
    - Range: $[-1.0154, 0.5507]$
- Quantum Model:
    - Mean attention: -0.0262 ± 0.2402
    - Range: $[-1.1238, 0.5643]$

2) Correlation Analysis: The correlation analysis between classical and quantum feature importance patterns showed:

- Pearson correlation coefficient: $r = -0.0425$ ($p = 0.2701$)
- The low correlation and non-significant p-value suggest that the models utilize fundamentally different feature representations

3) Spatial Distribution: The spatial distribution of feature importance revealed distinct patterns:

- Classical Model:
    - Concentrated attention in central regions
    - Primary focus points: $(7, 13), (21, 25), (3, 25)$
    - More localized feature utilization
- Quantum Model:
    - Broader attention distribution
    - Key attention points: $(25, 6), (2, 4), (17, 9)$
    - Greater emphasis on peripheral features

4) Regions of Maximum Difference: The largest disparities in feature importance were observed at coordinates:

Top differences at: $(24, 22), (0, 12), (8, 15), (1, 25), (24, 15)$
$$(5)$$

This analysis demonstrates that while the classical model tends to focus on traditional digit recognition features in central regions, the quantum model adopts a more distributed approach to feature processing. The near-zero correlation ($r = -0.0425$) between the models' feature importance patterns suggests they have developed complementary strategies for digit recognition, potentially explaining their different performance characteristics across various digit classes.
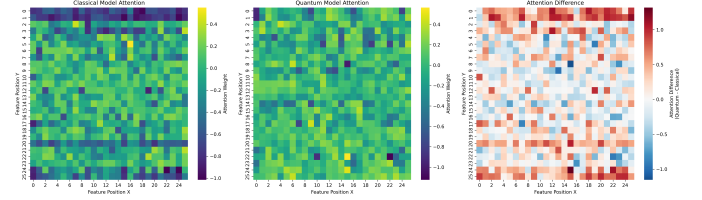

Fig. 10: Classical vs Quantum importance $I_j^{(e)}$.

XI. DISCUSSION

Quantum-encoded edge maps introduce noise that generally lowers overall accuracy and slows convergence (Fig. **??**). Yet in 7.10% of test samples, quantum preprocessing recovers critical edge structures missed by classical extraction (Table II), enabling correct NAM predictions (Fig. 3). The distributional analysis (Fig. 4) further highlights the classical pipeline's stability and precision over its quantum-inspired counterparts.

XII. CONCLUSION AND FUTURE WORK

Classical Sobel-like edge extraction remains the most reliable for MNIST with NAMs. Future directions include adaptive threshold learning, error-mitigation in QHED, and application to higher-resolution datasets.

REFERENCES

[1] Y. LeCun, L. Bottou, Y. Bengio, and P. Haffner, "Gradient-based learning applied to document recognition," *Proc. IEEE*, vol. 86, no. 11, pp. 2278–2324, Nov. 1998.
[2] Y. Zhang, M. Li, and Q. Su, "NEQR: A novel enhanced quantum representation of digital images," *Quantum Inf. Process.*, vol. 12, no. 8, pp. 2833–2860, 2013.
[3] P. Q. Le, F. Dong, and K. Hirota, "A flexible representation of quantum images for polynomial preparation, image compression, and processing operations," *Quantum Inf. Process.*, vol. 10, no. 1, pp. 63–84, 2011.
[4] Y. Li and J. Li, "Quantum Hadamard Edge Detection of Digital Images," arXiv:1703.04040, 2017.
[5] A. Agarwal, N. Frosst, X. Zhang, R. Caruana, and G. E. Hinton, "Neural Additive Models: Interpretable Machine Learning with Neural Nets," in *Adv. Neural Inf. Process. Syst.*, vol. 33, 2020.
[6] M. Rath and H. Date, "Quantum data encoding: A comparative analysis of classical-to-quantum mapping techniques and their impact on machine learning accuracy," *EPJ Quantum Technology*, vol. 11, no. 72, 2024.